Construction and Building Materials 150 (2017) 916–931

Contents lists available at ScienceDirect

Construction and Building Materials

journal homepage: www.elsevier.com/locate/conbuildmat

Evaluation of the response of a vaulted masonry structure to differential settlements using point cloud data and limit analyses

Sinan Acikgoz [a,*], Kenichi Soga [b], Jim Woodhams [c]

[a] Cambridge Centre for Smart Infrastructure and Construction, University of Cambridge, Cambridge, UK
[b] Department of Civil and Environmental Engineering, University of California, Berkeley, CA, United States
[c] Topcon Smart Infrastructure Business, Tokyo, Japan

HIGHLIGHTS

- Response of masonry vaulted structures to ground-induced settlements is examined.
- Algorithms proposed to obtain continuous 3D displacement fields from point clouds.
- Data from a settling masonry vault in London Bridge Station validates the algorithms.
- Limit analyses describe settlement response of the vault with accuracy.
- A new technique to predict support movement induced damage is proposed.

ARTICLE INFO

Article history:
Received 26 December 2016
Received in revised form 28 April 2017
Accepted 6 May 2017
Available online 27 June 2017

Keywords:
Masonry vault
Masonry arch bridge
Damage assessment
Laser scanning
Point cloud processing
Cloud comparison
Limit analysis
Settlement

ABSTRACT

Differential settlements have adverse effects on the serviceability and stability of vaulted masonry structures. However, the existing monitoring and assessment techniques do not capture these effects in sufficient detail. In this paper, a new approach is proposed to better describe the influence of support movements on barrel vaults. In this approach, laser scan point clouds of a settling vaulted structure are compared. Different cloud comparison methods are used to accurately identify the displacements of small point cloud segments. In particular, a new cloud comparison method, which modifies the well-known iterative closest point (ICP) registration algorithm, is developed. By constraining ICP to ensure displacement continuity between adjoining point cloud segments, three dimensional movement estimates of the structure are obtained. These estimates delineate the settlement response by indicating the location and magnitude of cracking. This rich information is then used to identify the settlement response mechanism of the vault using limit state numerical analysis. Finally, by interpreting the numerical results with relevant serviceability criteria, a new method to quantify the influence of settlements on barrel vaulted masonry structures is proposed. This damage assessment technique is used to evaluate observed damage due to piling-induced settlements in a masonry viaduct at London Bridge Station.
© 2017 The Authors. Published by Elsevier Ltd. This is an open access article under the CC BY license (http://creativecommons.org/licenses/by/4.0/).

1. Introduction

A major reason for differential settlements in urban areas is nearby underground construction works [1,2]. As excavation works are carried out, settlements and horizontal movements of nearby structures are inevitable. As a result, the differential movements in abutments, piers and foundations are a recurring problem for vaulted masonry structures [3–9]. These movements can threaten the structures' serviceability and stability and they need to be controlled.

Of particular concern are the serviceability issues, which arise as a result of differential movements. For instance, in masonry railway viaducts, differential settlements of piers may result in track deformations, causing changes in cant, twist and vertical alignment. It is important to measure and/or predict the displacement response at many locations in the vault to infer these movements. More generally, support movements may cause the formation of mechanisms in masonry vaults, which result in cracking. These cracks may deteriorate over time, due to environmental [10] and mechanical effects, such as fatigue and creep [11]. Therefore it is

* Corresponding author at: Department of Engineering, University of Cambridge, Trumpington Street, Cambridge CB2 1PZ, UK.
E-mail address: msa44@cam.ac.uk (S. Acikgoz).

http://dx.doi.org/10.1016/j.conbuildmat.2017.05.075
0950-0618/© 2017 The Authors. Published by Elsevier Ltd.
This is an open access article under the CC BY license (http://creativecommons.org/licenses/by/4.0/).

essential to quantify the location and magnitude of settlement-induced cracking.

Commonly used monitoring techniques provide limited understanding of structural response to settlements. Monitoring is achieved by tracking the absolute displacements of a number of discrete targets on the structure with total stations. Engineers use differential measurements between these sparsely placed targets to correlate the observed movements to damage levels [2,12]. However, as observed in a recent study, it remains difficult to reliably relate displacement signals from a few monitoring targets to serviceability limits or damage [13]. To quantify the influence of settlements, it is necessary to have a more detailed description of the displacement response of the vault.

The currently available settlement induced damage assessment techniques can be improved to become more reliable for vaulted structures. The assessment of settlement induced damage is often performed on the basis of highly uncertain estimates of ground movements. Further uncertainty and errors are introduced with the simplification of the mechanical representation of structures [14]. For instance, complex structures are typically represented with elastic beams and the damage in these models is quantified with semi-empirical techniques, which correlate the observed tensile strains to the magnitude and extent of cracking [1,2]. While these assessment tools may be effective for simple facades and framed buildings, it is shown in this study that they do not capture the mechanical behaviour of more complex vaulted masonry structures.

To overcome these challenges, alternative approaches for monitoring and assessing settlement-induced damage in masonry vaulted structures are proposed in this study. Primarily, this entails a new monitoring technique, which utilises several laser scan point clouds of the structure, collected during ground works. The point cloud data is processed with a range of techniques including primitive shape fitting [15], cloud-cloud distance comparison [16] and rigid body cloud registration [17] to infer displacements from point clouds. With this approach, instead of measuring the displacement of a few discrete points on the structure, 3D displacements of all visible surfaces on the intrados of the arch can be obtained. Then, by using this information, it is possible to track the rotation and lateral displacement of piers as well as continuous longitudinal and transverse displacement profiles of the arch barrel. This rich information allows a conservative estimation of emerging crack opening and track displacement parameters, which are useful for determining the serviceability of the investigated structure. The displacement data is also useful for investigating the accuracy of simple modelling tools, which may be used in lieu of the aforementioned beam methods to capture the settlement response behaviour. For this purpose, the paper examines the accuracy of a simple limit analysis based damage assessment approach. The utility of this modelling approach for providing a preliminary damage assessment for a given support settlement is also explored.

The paper is organised as follows. First, a case study from the London Bridge Station redevelopment project, is described in Section 2 to introduce the current techniques of monitoring and assessing settlement-induced damage and discuss their shortcomings. Then, a new monitoring technique, which utilises point clouds, is developed in Section 3. For the development, the accuracy of established methods of cloud comparison and registration techniques are evaluated, highlighting the difficulties in estimating accurate displacements using these methods. Suitable modifications to these techniques are then proposed to develop point cloud data processing algorithms which provide continuous 3D deformation profiles. Such information is particularly useful for estimating damage due to movements. On the basis of these results, new mechanical models for damage assessment are proposed in Section 4. These models are based on limit analyses of masonry arches and provide direct indicators of damage. Finally, upon validating these models with point cloud data, new damage assessment maps are proposed for settlement-induced damage in vaulted masonry structures in Section 5.

2. The case study

London Bridge Station is a historic railway station composed of a series of brick-built viaducts, originally constructed in various phases during the 19th century. As a part of the recent redevelopment works involving removal and replacement of sections of the viaducts, new piles were constructed in these viaducts, whilst the tracks above remained operational. The piles formed the foundation of buttress walls, which were constructed later. These buttress walls were designed to take the thrust from neighbouring barrel vaults after the demolition of a part of the masonry viaduct for the construction of the new station. This sequence of construction is schematically illustrated in Fig. 1a. The critical investigation phase which caused significant settlements is the piling phase, Phase 1. The piles were constructed in Arch E55 but this case study will examine the neighbouring Arch E57, which was not demolished.

The location and construction sequence of piles is illustrated in Fig. 1b. All piles were 0.45 m in diameter, 25 m in length and were constructed using a segmental flight auger. The construction of piles started on 31.01.13 from the north and progressed towards the south. Piling works finished on 16.08.13. In this period, 105 piles were constructed. Construction of buttress walls followed shortly after, and was completed before 21.11.13.

Fig. 2 illustrates the internal construction of the examined Arch E57 with a longitudinal section view. The barrel vault has a square span of 9.6 m and a rise of 2.2 m. The multi-ring arch is well-bonded and is 0.7 m thick. It is supported by 1.6 m thick piers of solid brick. Above the piers is 1.9 m backing and 1.4 m well-compacted soil fill, which together support the track ballast. It is noteworthy that a bitumen waterproofing layer exists between the fill and the backing, which is designed to divert the draining water to discharge from the piers. The piers themselves are supported on shallow foundations of lime concrete, which bear onto alluvial ground.

The plan view in Fig. 3a shows that Arch E57 has a width of 27 m. Two cross-passages allow access to the neighbouring arches and are located centrally. Fig. 3a also highlights six longitudinal sections, shown with dashed lines, where monitoring targets were placed. Two of the six longitudinal sections monitored with total stations are highlighted. The one in the north is labelled L1 and the one in the south is labelled L2. In addition, T1, a transverse section of the bridge, running along its crown, is also highlighted.

In each longitudinal section, monitoring targets were placed at the eastern and western springing points and the crown. Monitoring results for the section L1 are demonstrated with vector plots in Fig. 3b, where the lateral and vertical movements in the longitudinal plane are respectively denoted by ΔX and ΔZ. The transverse deflections ΔY are not reported, as they were negligible. The top row of Fig. 3b shows the recorded movements of targets (in mm) on 05.03.13, by which time 50% of the piles in Arch E57 had been constructed. The bottom row shows the recorded movements on 23.11.13, after the construction works finished. As expected, significant vertical settlements are observed on the western side for both dates. This movement is accompanied by considerable lateral movement of the pier top. However, negligible movement is observed on the eastern springing.

The monitoring data in Fig. 3b is analysed further in Table 1. In this table, the differential vertical settlement of piers (denoted by Δp_v) and the span change due to differential lateral movements (denoted by Δp_h) are reported. The results from L1 and L2 are

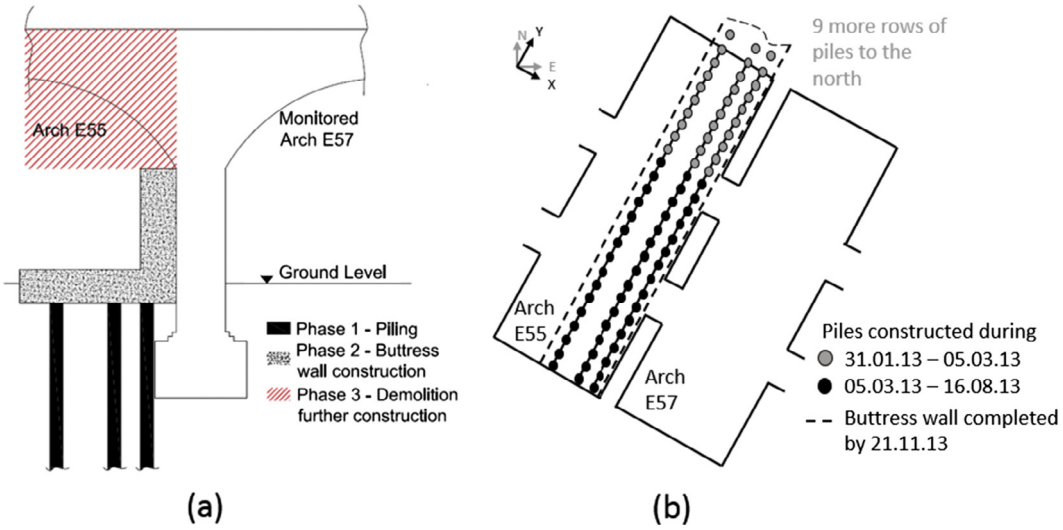

Fig. 1. (a) Schematic and (b) plan view illustrating the piling, buttress wall construction and demolition works which caused settlements in the masonry arch E57.

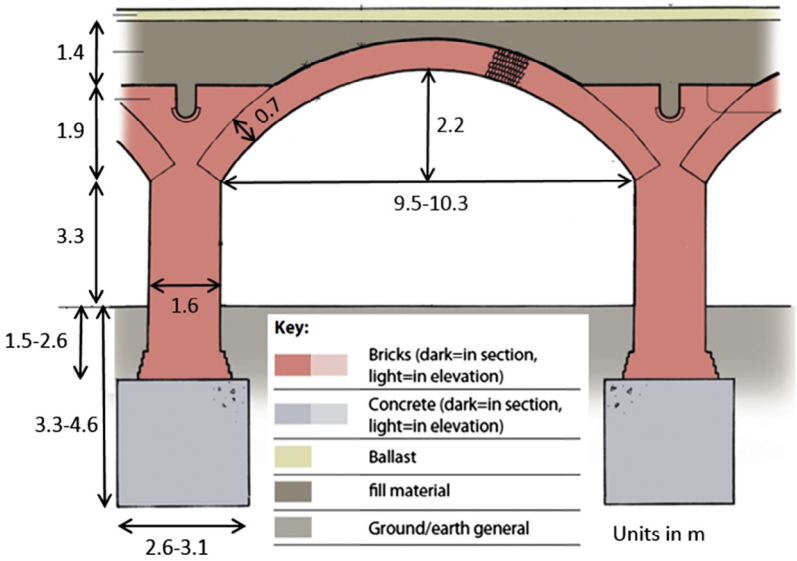

Fig. 2. Section view illustrating the internal construction and likely dimensions of Arch E57 (Modified from an original drawing by Alan Baxter Associates [18]).

similar, indicating that the piling-induced settlements were spread over a large area. Therefore, the following discussions will only focus on data from L1.

The differential vertical settlement for L1 increases from 23.1 mm to 42.7 mm in the investigated period. This corresponds to a similar increase in the deflection ratio, which is defined as the differential vertical movements normalised by the span length. However, the corresponding angular distortion during the same period demonstrates a small decrease. Angular distortion, β, is a measure of the relative movement of the crown with respect to the springing points [12]. It is calculated using the following formula for the longitudinal section:

$$\beta = \frac{|2\Delta Z_C - (\Delta Z_{WS} + \Delta Z_{ES})|}{L} \quad (1)$$

where ΔZ_C, ΔZ_{WS} and ΔZ_{ES} are the vertical movements experienced by the crown, western and eastern springing points. L is the span. In the investigated case, the crown movement is roughly proportional to the differential vertical settlement of the piers. This explains why negligibly small angular distortions of 0.00014 and 0.00011 were calculated for section L1 during and after piling.

On 05.03.13 and 23.11.13, a span opening of approximately 5 mm is recorded for L1. Fig. 3b indicates that significant lateral movements of both piers are observed between these two dates, which do not appear to cause further span opening. Therefore, the horizontal strain, defined as the ratio of span change and span length, remains approximately the same for both dates. At this stage, the displacement measurements by total stations demonstrated daily fluctuation of +-3 mm and this may have affected the results.

The angular distortion and horizontal strain values from Table 1 were utilised for the calculation of a damage category by the engineers [19]. The underlying assumptions which are used to relate displacements to damage are discussed in [12] but are briefly summarised here. These assumptions are derived from Boscardin and Cording's seminal study [2], where the structure undergoing settlement and horizontal movement is represented by an elastic deep beam with a height to length ratio of 1. The maximum strains experienced by the beam due to the observed relative deflections

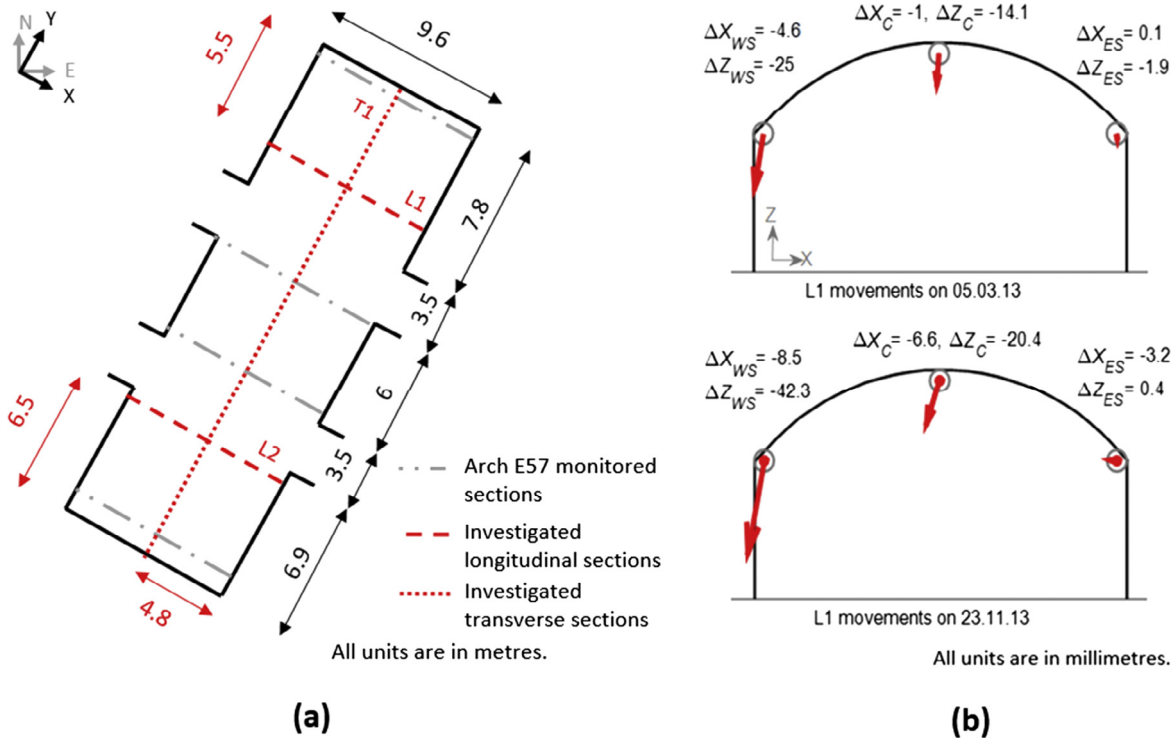

Fig. 3. (a) Plan and (b) section views of Arch E57 illustrating the location of monitored sections. In particular, (b) shows the movements records by total stations due to piling works.

Table 1
Critical differential settlement parameters recorded by total stations.

	Date	Differential vertical settlement of piers Δp_v (mm)	Deflection ratio, $\frac{\Delta p_v}{L}$ (%)	Angular distortion β (rad)	Span change Δp_h (mm)	Horizontal strain, $\frac{\Delta p_h}{L}$ (rad)	Damage category
L1	05.03.13	23.1	0.24	0.00014	4.7	0.00049	Very slight
	23.11.13	42.7	0.45	0.00011	5.3	0.00055	Very slight
L2	05.03.13	21.1	0.22	0.00047	4	0.00042	Very slight
	23.11.13	42.2	0.44	0.00031	5.2	0.00055	Very slight

are calculated with closed-form equations which use the angular distortion and horizontal strain as input. Then, by comparing the maximum experienced strains with previously categorised values of limiting tensile strain [1], a damage category is calculated. This damage category is expected to relate to the width and extent of cracking. For instance, very slight damage is experienced when the calculated tensile strain is between 0.05 and 0.075% and the crack width is less than 1 mm. These limiting strain values and the crack widths were empirically defined [1].

Utilising this approach for a longitudinal section of the masonry vault suggested very slight damage, as the observed horizontal strains and angular distortions were smaller than the slight damage category thresholds, which are respectively 0.0008 and 0.0016 rad. Ordinarily, the very slight damage state would indicate cracking less than 1 mm [1]. However, the calculation of negligible angular distortions for significant vertical settlements indicates the unsuitability of this method. More appropriate mechanical models are proposed to tackle this issue in Section 4.2 of this paper.

As shown in Fig. 4, significant vertical and horizontal movements induced by piling were detected by engineers. An alarm was triggered when the crown displacements exceeded 20 mm in Arch E57. The following visual inspection of the vault revealed that, contrary to the very slight damage state calculated in Table 1, the arch sustained notable cracking, particularly on the western side. This transverse intrados crack is sketched in the plan view of Arch E57 in Fig. 4a where it extends throughout the transverse length of the vault. Around this crack, water patches could be observed. These patches indicate that the arch response mechanisms have disturbed the waterproofing layer located between the arch and the fill (see Fig. 2). As a result, water appears to drain in the vicinity of the induced crack. On the eastern side of Arch E57, existing cracks were visible but no new crack formation was observed. However, abundant water patches in this region are indicative of a potential extrados crack.

The emerging cracks did not pose any stability issues and the trains were permitted to continue operation as usual during this period. However, in order to better understand the observed damage, further work was required. In the following section, new point cloud monitoring techniques are developed to achieve this.

3. Point cloud monitoring

Laser scanning is a non-destructive, non-contact and precise distance measurement technology. Along with structure-from-motion digital photogrammetry techniques [20], it is used to generate three dimensional point clouds of the structure. In the last decades, point cloud data has found new uses in the evaluation of historic masonry structures. The applications range from the detailed documentation of historic buildings [21,22] and structural geometry [23–25] to the identification of material damage [26] and

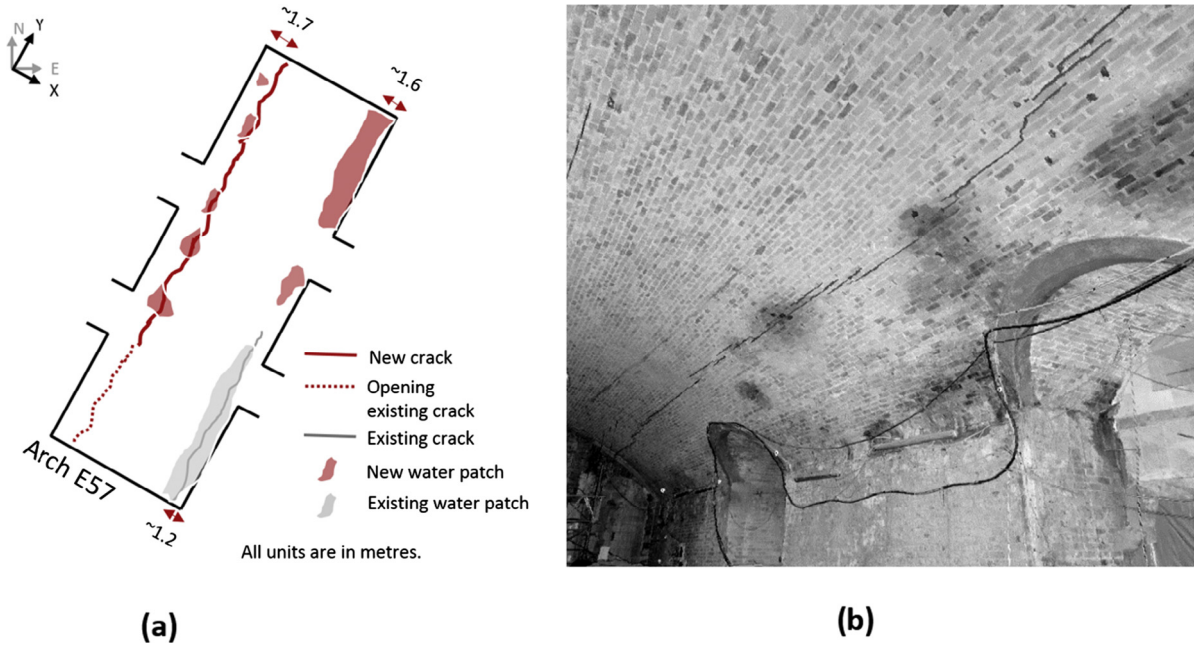

Fig. 4. (a) Plan view and (b) photo demonstrating the damage sustained by the masonry arch E57 during piling work, in the form of cracking and water patches. The photo shows the central and southwestern section of Arch E57.

geometric anomalies [15,27]. There has been recent use of point cloud data for structural health monitoring of masonry assets [28,29], but these have been few in number.

In order to monitor the asset, laser scan surveys of Arch E57 were made before, during and after piling using a commercial laser scanner by the contractor [29]. In the text, point clouds from these surveys may be referred to as 'before piling', 'during piling' and 'after piling' point clouds. The plan view of a sample point cloud that was obtained is shown in Fig. 5a (top). Then, in Fig. 5a (bottom), the dates, numbers and corresponding piling completion rates for these scans are specified. It is noteworthy that these scan dates correspond to the dates for which total station monitoring data was examined in Section 2. In the current section, point cloud data from these dates are compared.

To ensure successful point cloud comparisons, certain data collection and data processing requirements needed to be met. These requirements are described in Table 2, alongside the workflow that was adopted. Upon the application of the items 1–5 of this workflow, point cloud slices of sections L1 and L2 (see Fig. 2) were obtained for each point cloud. As an example, the slice L1 of the 23.11.13 (after piling) point cloud is shown in Fig. 5b. Here, the colour of individual points is determined by laser intensity returns. Following this, the slice was segmented into smaller units, in accordance with item 6 of the workflow in Table 2. This segmented

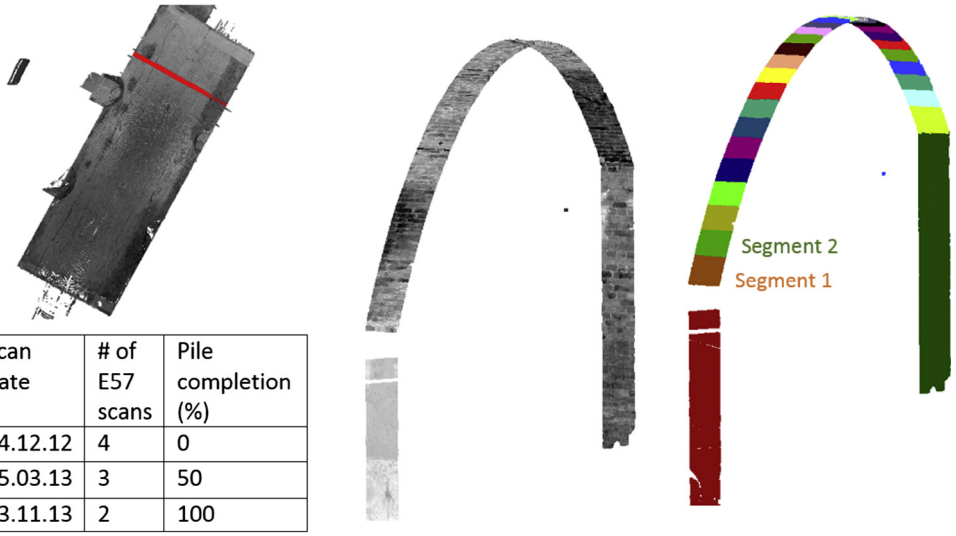

Scan date	# of E57 scans	Pile completion (%)
14.12.12	4	0
05.03.13	3	50
23.11.13	2	100

Fig. 5. (a) Top view of a registered laser scan point cloud of Arch E57 with a table indicating the scan date, number of scans and corresponding piling status. Perspective view of the monitoring section L1 (b) after the point cloud is processed and (c) segmented.

Table 2
The observed workflow for data collection and processing point clouds for cloud comparison.

Workflow	Requirements	Application
1 – Data collection	High scan density is needed for accurate cloud comparison.	Faro Focus X330 was used with a minimum of 2 scans.
2 – Registration	Robust tie-point registration with well-spread targets is necessary	Minimum of 3 sphere targets linked the scans. Coordinates of 3 of these were determined by survey
	A well-maintained survey network with high quality control points is essential for georeferencing	Georeferencing errors less than 2 mm were achieved in the software FARO Scene
3 – Denoising	Outliers and out of range laser scan points need to be eliminated	Statistical outlier removal filters are utilised in the software Cloud Compare
4 – Cleaning	Features which are not investigated (e.g. floors) and which are not in both scans (e.g. a new pipe) need to be removed	Segment tool in Cloud Compare is used manually for this purpose. This can be done after data slicing
5 – Data slicing	Data slices along longitudinal and transverse axes facilitate structural analysis	30 points were picked along the crown bedding joint and the best-fitting line defines the transverse axis
	To identify features which define these axes (e.g. a bedding joint), laser scan intensity data is necessary.	Perpendicular longitudinal axes were then defined to extract slices in locations L1 and L2 (see Fig. 3a).
6 – Data segmentation	Pier and vault components need to be segmented	Abrupt changes in surface normals were used for segmenting piers and the vault
	The vault needs to be divided into sections of equal arc length	The vault slice was modelled as an ideal cylinder, before unrolling it and dividing it into sections of approximately equal arc length of 0.35 m, corresponding to 5 bricks

point cloud is shown in Fig. 5c, where each segment is shown with a different colour. Each segment is also given a numerical ID, with the westernmost segment being named as Segment 1, the next one Segment 2, etc. As a result of this workflow, small georeferenced point cloud segments of slices L1 and L2 were retrieved for all examined dates. Georeferencing was done with respect to control points established outside the zone of influence of ground works, using the London survey grid.

The processed data was then used to determine displacements using two cloud comparison methods. The first method computes distances between clouds in desired directions using the M3C2 (Multiscale Model to Model Cloud Comparison) method [16]. In certain cases, these distances can be used to estimate the displacements. The second method is called the Piecewise Alignment Method (PAM) [17]. Here, it is necessary to identify the corresponding sections of data from different point clouds and register them to one another. This registration provides the translational and rotational rigid body movements of the cloud between two dates and allows the definition of displacement fields for all investigated points.

3.1. Application of the M3C2 method

The objective of the M3C2 method is to accurately determine the distance between two point clouds in a desired direction. The measurement direction is described by a unit vector. For this example, a vertical vector can be considered. The first step of the analysis is to specify a core point where the analysis will be conducted. Then, by projecting a vertical cylinder with a radius R which passes through the core point, the points which remain in the cylinder are identified for both clouds. Following that, the average positions of the identified points in each cloud are identified. The difference between the elevations of these average positions gives the vertical distance between clouds.

The process of averaging points within the cylinder is designed to minimise distance measurement errors which arise due to laser scan ranging error. Due to this, the M3C2 method is particularly useful when comparing two (approximately) flat surfaces. Two such surfaces are represented with noisy point clouds in Fig. 6a. The second point cloud represents the same object as the first point cloud, but it has been vertically displaced by Δ_v. The M3C2 method can accurately determine this distance with minimal noise, due to its averaging of points. In Fig. 6b, an alternative case is examined when the second point cloud has moved laterally by Δ_h, following its vertical displacement. If the surface is flat, the lateral movements do not impact on the M3C2 estimation, which can still estimate the vertical displacement Δ_v well.

However, when a curved surface is considered, the relationship between M3C2 estimations and vertical movements is less clear. Consider the curved point clouds in Fig. 6c, which represent the same curved surface, but one of them has been vertically displaced. Here, the M3C2 method will be able to capture the vertical distance between clouds, but with significantly more noise than the first examined case of a flat surface. The reason for this is the averaging of the elevation coordinates of points in a curved surface, which inevitably results in more noise than on a flat surface. Next, consider the case in Fig. 6d, where the second curved cloud is displaced vertically by the same amount Δ_v and then displaced horizontally by Δ_h. The displacement of Δ_h causes a reduction in the vertical distance between the curved clouds. Therefore, for the specific case shown in Fig. 6d, the M3C2 estimation Δ_{M3C2} will be smaller than Δ_v. The magnitude of this difference between the M3C2 estimation and the vertical deflections depends on the orientation of this cloud.

The previous discussions point out the limitations of the M3C2 method in estimating vertical displacements for curved surfaces. The influence of these limitations is demonstrated in Fig. 7 where total station and point cloud monitoring data from Arch E57 is investigated. Fig. 7a shows the displacements estimated by comparing the longitudinal slice L1 retrieved from before and after piling clouds using the M3C2 method. In the M3C2 analysis, a radius R of 5 cm was utilised. The raw M3C2 data has been filtered with a Savitzky-Golay filter and both of these data sets are presented. In Fig. 7b, the standard deviation of the points considered for the M3C2 analysis are plotted. Fig. 7b demonstrates that the noise in the M3C2 data induced by averaging the elevation coordinate of points in curved surfaces is significant. According to Fig. 7b, a standard deviation close to 15 mm is observed at $X = 0$ m and $X = 9.6$ m, near the springing points. Conversely, this standard deviation is approximately 2 mm at the crown around $X = 4.8$ m, where the vault is the flattest. This explains the significant noise observed in the Fig. 7a for the raw M3C2 results around the springing points. The noise is significantly less at the crown.

When the displacement estimates from the M3C2 method and total station data are compared in Fig. 7a, it can be observed that the M3C2 method estimates at the crown are accurate. Here, the cloud is flat, and the vertical displacements are captured. However, around the western springing point, the M3C2 method estimates

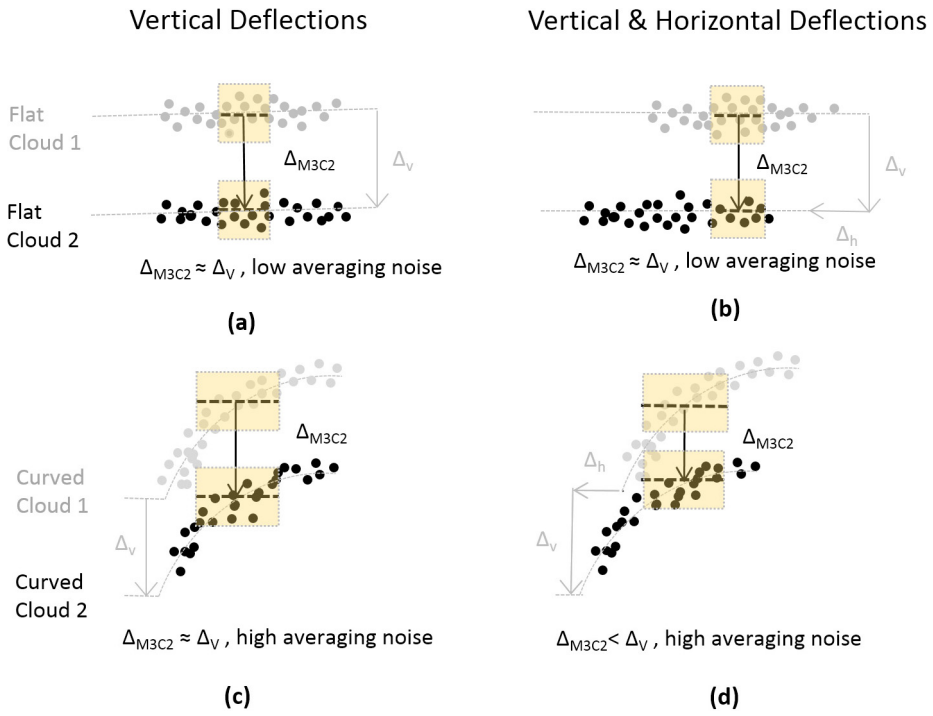

Fig. 6. An illustration of M3C2 distance estimations for vertically and horizontally translating point clouds representing (a-b) flat and (c-d) curved surfaces.

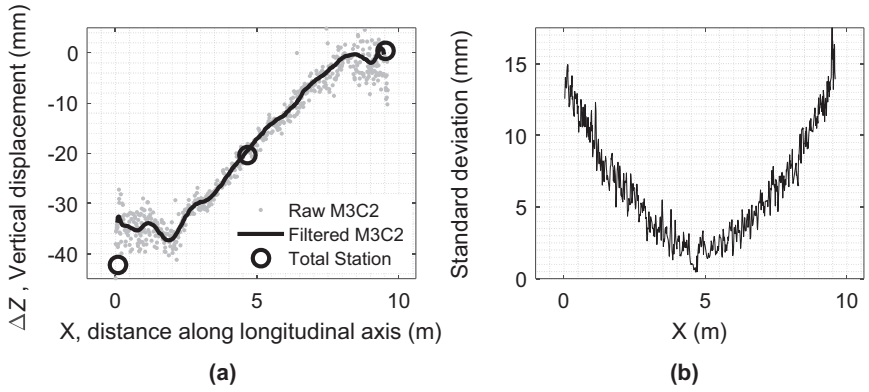

Fig. 7. (a) Vertical displacements estimated for the slice L1 after piling on 23.11.13 using the M3C2 method and total station data and (b) standard deviation of Z coordinates of points used in M3C2 analyses.

10 mm less vertical movement than the total station data. This is due to the lateral movement of the western springing point, which was measured as 8.5 mm in Fig. 2. This lateral movement causes the vertical distance between clouds to get smaller, and the M3C2 method can no longer accurately estimate the vertical displacements observed in the vault.

Fig. 7 demonstrates that determining the distance between clouds is not sufficient to estimate vertical displacements of curved surfaces around springing points. However, it also demonstrates that the M3C2 method is reliable when determining vertical displacements of flat surfaces, such as locations around the crown. In Fig. 8a, the vertical displacements of the crown of the arch are plotted against distance along the transverse axis of the arch, along the highlighted section T1 (see Fig. 3 for the location of this section). Similar to Fig. 7a, the raw and filtered M3C2 data, and total station measurements are shown in Fig. 8a. Results show that the M3C2 data is in good agreement with the total station data. The M3C2 data generally remains within the 3 mm error band of the total station data, and does not demonstrate significant changes along the transverse length. In Fig. 8b, the standard deviation of the points considered for the M3C2 analysis are plotted. Similar to the crown data from Fig. 7, the standard deviation of points fluctuates around 2 mm.

The examples presented until this point have explored the use of the M3C2 method for estimating vertical deflections. However, the M3C2 method can also be used to determine displacements of vertical surfaces in the horizontal direction. In order to estimate the lateral deformations experienced at the top of the pier, the M3C2 method is utilised with a radius *R* of 5 cm. Then, an average M3C2 estimate was obtained and is reported in Table 3. Alongside the mean value of the M3C2 estimate, its standard deviation is also reported. The comparison between the lateral movements estimated from the M3C2 method and the total station are similar, particularly for L1. Some differences are observed in the lateral movements of springing points of L2. However, the total span opening estimated by the M3C2 method and total station data

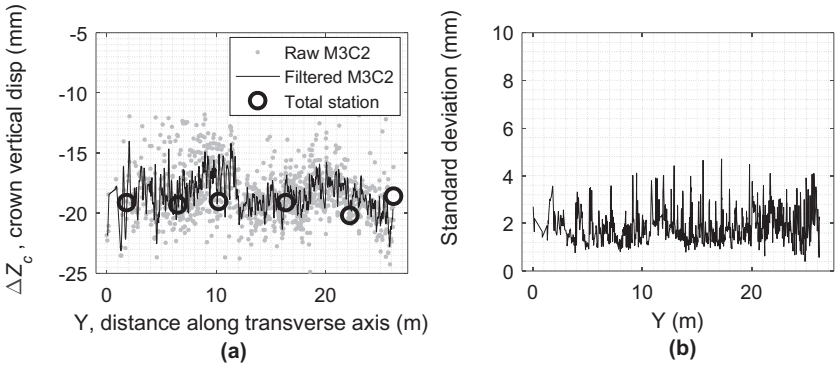

Fig. 8. (a) Vertical displacements estimated for the slice T1 on 23.11.13 using the M3C2 method and total station data and (b) standard deviation of Z coordinates of points used in M3C2 analyses.

Table 3
The lateral movements at western and eastern springing at the L1 and L2 sections.

	Date	ΔX_{WS}, west pier springing lateral movement (mm)		ΔX_{ES}, east pier springing lateral movement		M3C2 span change (mm)	Total station span change (mm)
		M3C2	Total Station	M3C2	Total Station		
L1	05.03.13	−5.4 ± 3.5	−4.6 ± 3	−0.3 ± 2	0.1 ± 3	5.1	4.7
	23.11.13	−7.7 ± 1.5	−8.5 ± 3	−2.6 ± 1.8	−3.2 ± 3	5.1	5.3
L2	05.03.13	0.8 ± 3	−1.2 ± 3	2.8 ± 1.2	2.8 ± 3	2	4
	23.11.13	−5.3 ± 3.8	−10.2 ± 3	−1.8 ± 2.4	−4.9 ± 3	3.5	5.2

are similar. This validates the accuracy of using the M3C2 method for estimating deflections of flat surfaces in the direction of their surface normal.

3.2. Application of the PAM method

The Piecewise Alignment Method (PAM) registers segments of point clouds to one another [17]. To do this, it uses the well-known ICP (Iterative Closest Point) algorithm [30]. In the current implementation, the ICP code that was written by [31] was modified for purpose.

As a result of the workflow presented in Table 2, small segments of the slices L1 and L2 were obtained from the point clouds obtained on three different dates. For instance, the 0.35 m long vault segment that springs from the western pier, was named as Segment 1 (see Fig. 5c). In the PAM, the ICP algorithm was applied to the point clouds of Segment 1 from different dates. It is noteworthy that these point clouds 'correspond' to the same sections of the vault, however, they may be slightly different. Two such point clouds, representing the same segment at two different dates are shown in Fig. 9a.

The ICP algorithm initiates by establishing correspondences between points. In the absence of further information, the algorithm assumes that each point corresponds to its nearest neighbour in the other cloud. For instance, for the grey and black point clouds shown in Fig. 9a, the closest distance for a point in the black cloud can be found by projecting the surface normal from that point to the grey cloud. These 'corresponding' points are then processed further and stored in a matrix. Once this is achieved for all points, the singular value decomposition of the matrix is evaluated. This provides the elementary rotations and translations required to register the black point cloud to the grey point cloud. This process is repeated until the black cloud converges to the grey cloud. This is achieved typically within 5 iterations and the end result of the application of the ICP algorithm is shown in Fig. 9b.

Fig. 10 shows the results of the application of the PAM method to the before piling and after piling point cloud slices of L1. Fig. 10a and b plot the calculated vertical and lateral displacements of small point cloud segments along the longitudinal axis. Displacement data from total stations is also plotted for comparison. Fig. 10c shows the in-plane rotation of segments while Fig. 10d summarises the results by plotting the deflected shape.

The results in Fig. 10a and b demonstrate that the western springing displacements calculated using the PAM method are very different compared to the total station measurements. The vertical movement is underestimated by about 20 mm by the PAM method. At the same location, the PAM method predicts lateral movements in the opposite direction to those indicated by the total station data. The vertical and lateral movement measurements at the crown and eastern springing points agree better. However, the discontinuities in the lateral displacement trace are pronounced (for instance at $X = 3.5$ m) and need further exploration.

The ICP method establishes an arbitrary correspondence between point clouds by matching the nearest neighbouring points between clouds. This results in the black point cloud moving roughly in the direction of its surface normal to match the grey cloud in Fig. 9a. As a result, the lower edges of the black and grey clouds do not match in Fig. 9b. The same phenomenon is observed in Fig. 10 for Segment 1, which springs from the western pier wall. The undeformed point cloud moves 18 mm in the X direction and −15 mm in the Z direction to match the deformed point cloud. The indicated movement is arbitrary and does not relate to the physical movement of the segment. The observed discontinuities in the lateral displacement trace also arise from this arbitrary method of establishing correspondences between clouds.

In order to correct these systematic errors, some modifications are proposed to the PAM method in this study. These modifications are aimed at ensuring that better correspondences are established between points. This entails constraining the ICP to provide displacement continuity between different segments. The method that was used to achieve this is given the name Iterative PAM (IPAM), and is graphically explained in Fig. 9c and d.

Before starting the ICP algorithm, the undeformed black point cloud is subjected to an initial alignment in the proposed IPAM

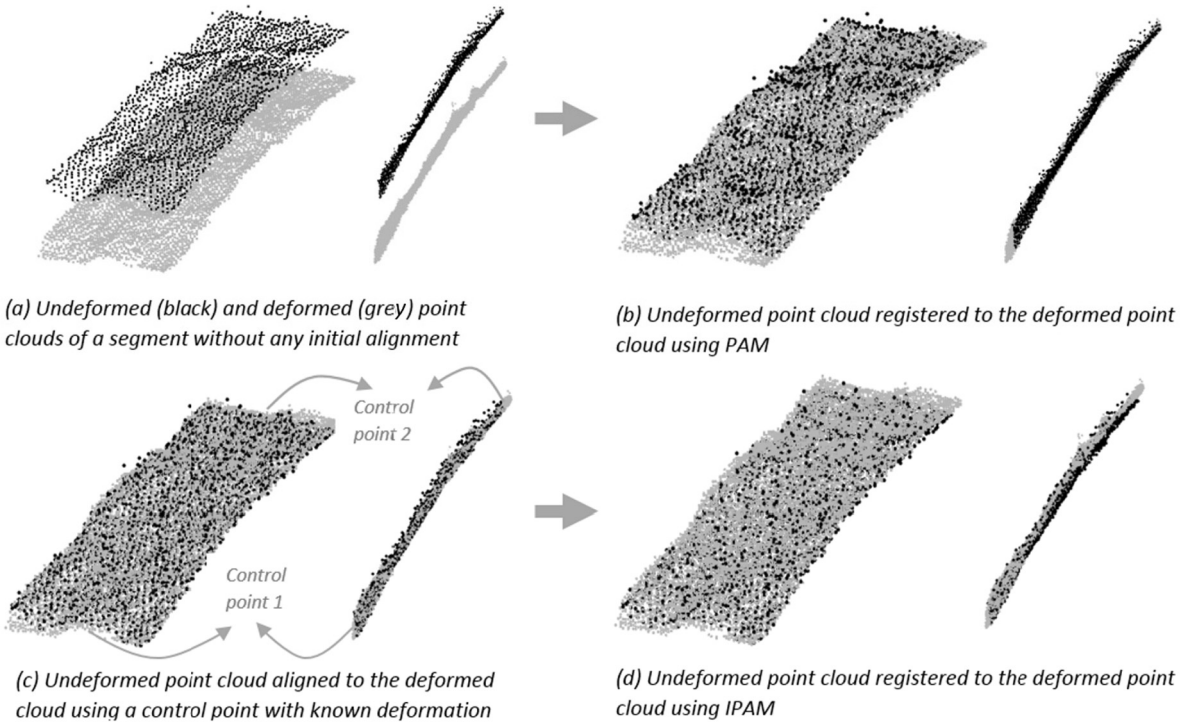

Fig. 9. (a-b) An application of the PAM method to a segment of the point cloud and (c-d) an application of the improved IPAM method to the same segment.

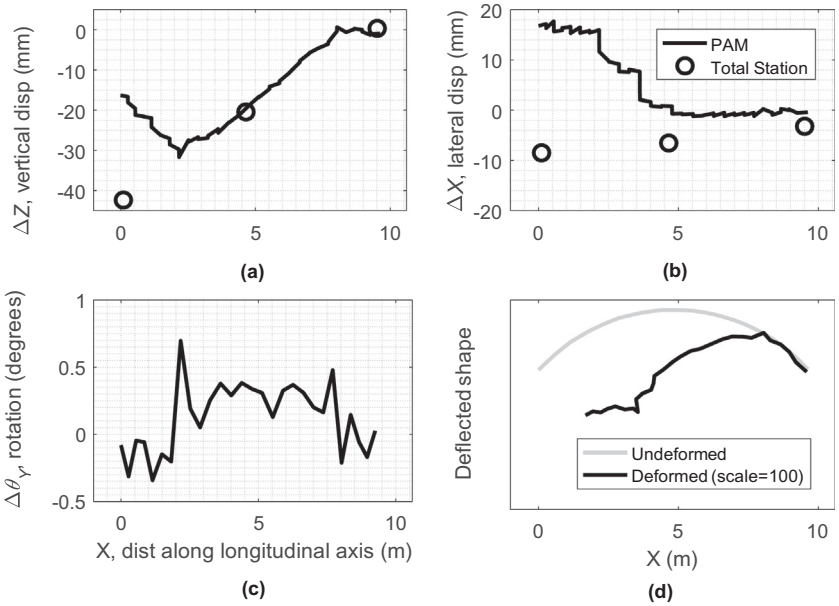

Fig. 10. An application of the PAM method to the 'before piling' and 'after piling' point cloud slices L1 retrieved on 14.12.12 and 23.11.13. Calculated (a) vertical and (b) lateral displacements, (c) in-plane rotations and (d) the deflected shape of L1 are shown.

approach (Fig. 9c). This initial alignment is based on the (partially) known movement of a control point 1, which is located approximately in the middle of its 'starting' edge. For instance, for Segment 1, the lateral movement of the control point 1 can be estimated from the lateral movement of the pier top, which was calculated in Table 3. Alternatively, for an arbitrary segment j, the movement of the control point 1 can be estimated from the movement of the connecting edge of the adjoining segment $j-1$. If the ICP algorithm is applied after this initial alignment, the rest of the black cloud rotates about the control point to match the grey cloud while the control point typically moves very little. However, if the control point movement is altered during the ICP registration the initial alignment is varied and the process repeated until the known movement of the control point is recognised by the ICP algorithm. The clouds registered using this procedure are shown in Fig. 9d. If the black cloud registered using the proposed IPAM method is contrasted with the black cloud registered using the PAM method, it can be seen that the proposed IPAM method causes the black cloud to move further down. After the registration is complete, the movement of control point 2, which is located approximately in

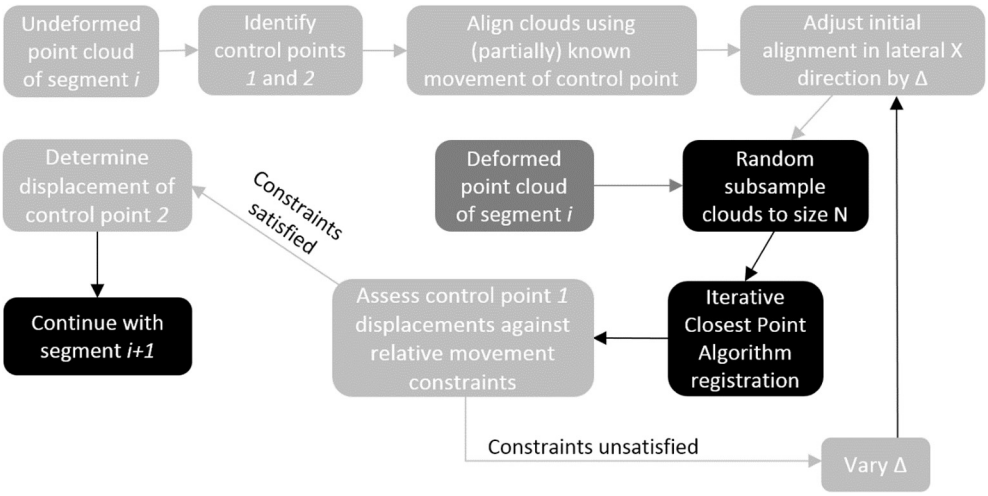

Fig. 11. Schematic description of the proposed IPAM algorithm.

the middle of its 'ending' edge, is determined. This movement is used to define the movement of the control point 1 of the next segment, and the process is repeated.

The schematic description of the proposed IPAM algorithm is provided in Fig. 11. In the figure, the light and dark grey boxes describe operations on the undeformed and deformed point clouds, while the black boxes indicate operations on both clouds. Some additional details concerning the numerical implementation of the algorithm is provided in the figure. An important aspect is the constraint values that are specified for determining if the ICP registration has been successful. While iteratively registering each segment, the algorithm checks if the movement of the control point 1 of the current segment complies with the (partially) known movement of the corresponding control point 2 of the previous segment. If the calculated movements in the X and Z directions are within 0.25 mm and 1 mm of the known movement, then the algorithm accepts the registration and proceeds onto the next segment. If not, the initial alignment is varied by an amount of Δ in the positive and negative X directions. At each step, the amount of variation differs, but the variation is incrementally applied in steps of 0.25 mm until a successful registration is achieved.

An implementation of the IPAM algorithm in MATLAB can be found in an online open data repository, alongside the raw data files used for the analyses in this paper (see Acknowledgements section). The computational efficiency of the algorithm relies on the specific ICP algorithms and parameters used for the IPAM method [32] as well as the aforementioned constraints. However, for this case study, each application of the ICP algorithm achieved convergence in three-four iterations. In order to achieve displacement continuity between segments, the ICP algorithm was applied iteratively on datasets with slightly different initial registrations (see Fig. 11). On average, four iterations of initial registration were necessary before achieving a registration that satisfied displacement constraints.

The specified constraints allow an efficient and accurate calculation of the displacements experienced by the structure using the new IPAM method. This is demonstrated in Fig. 12, where the method is applied to the before piling and after piling point cloud

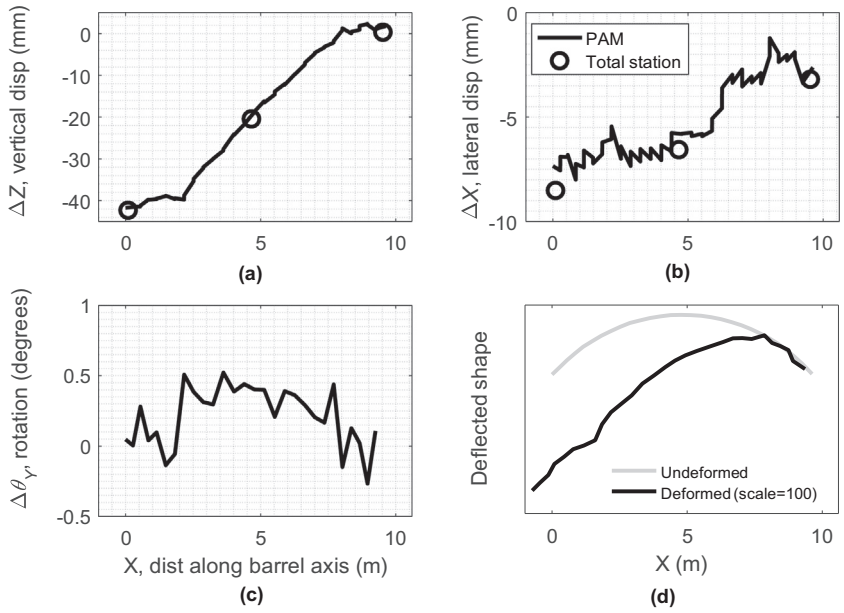

Fig. 12. An application of the proposed IPAM method to the 'before piling' and 'after piling' point cloud slices L1 retrieved on 14.12.12 and 23.11.13. Calculated (a) vertical and (b) lateral displacements, (c) in-plane rotations and (d) the deflected shape are shown.

slices of L1. Compared to the previous methods, the proposed IPAM method demonstrates a better agreement with the total station data. In particular, the vertical and horizontal displacements around the western springing point, which could not be reliably estimated by the M3C2 and PAM methods, are captured with an accuracy of 1 mm. The horizontal and vertical displacements at the crown and eastern springing point displacements are also captured with a similar accuracy. Furthermore, it is also noteworthy that the displacement discontinuities observed in Fig. 10 for the PAM method, effectively disappear in Fig. 12. The stringent constraints that ensure vertical displacement continuity have resulted in smooth vertical displacement profiles. The lateral displacement continuity criteria were less stringent, and minor displacement discontinuities are observed in Fig. 12b.

Having validated the accuracy of the proposed IPAM technique, the following section investigates the structural implications of the continuous displacement traces revealed using this method.

4. Investigation of structural response to settlements

4.1. Interpretation of structural response

The application of the proposed IPAM method to the 'before piling' and 'after piling' point cloud slices of L1 revealed an interesting displacement trace in Fig. 12. In particular, the vertical displacement trace in Fig. 12a clearly shows three approximately straight lines. This suggests that the vault accommodates the settlements by allowing three different macro-blocks to rotate with respect to one another. This argument is supported further by the in-plane rotation trace in Fig. 12c. Although the data is noisy, three sections of data with different values of rotation are evident in the trace. The western and eastern sections with X coordinates 0–2.15 m and 8–9.15 m rotate very little, whereas the central section demonstrates a consistent in-plane rotation of approximately 0.45°.

Before exploring the structural implications of these displacement traces, it is useful to investigate if similar traces are observed for point clouds from different dates. In Fig. 13a and b, the vertical and horizontal displacement traces obtained using the proposed IPAM method for the slice L1 are presented. The results from two dates, where 50% and 100% of the piling work was completed, is presented. In both data sets, the vertical displacement trace appears to be constructed of three different straight lines. These lines appear to meet at the coordinates $X = 2.15$ m and $X = 8$ m, where changes of slope are observed in the vertical displacement trace. In comparison, the magnitudes of lateral displacements are significantly smaller, and a similar trace composed of three lines is not observed for the 'during' piling point cloud.

Fig. 13c and d further investigate if a similar vertical displacement response is observed in both of the investigated slices L1 and L2. Their response on 05.03.13 is compared for this purpose. It is at this piling stage that the responses may be expected to be different, as the constructed piles are situated at the north, close to L1 (see Fig. 1). However, the vertical displacement responses are similar. As discussed earlier, this indicates that the settlements due to piling were spread over a large area of the vault, resulting in similar vertical displacement traces for L1 and L2. However, notable differences still exist between the settlement response at L1 and L2. In particular, the kink in the vertical displacement trace is around $X = 2.5$ m for L1 and $X = 2$ m for L2. This may indicate that the response mechanism in L1 and L2 is different. This can be explained by the distinct lateral displacements observed in these sections (see Fig. 13d). While significant lateral displacements and notable span opening is observed for the L1 section, there appears to be negligible lateral movement for the L2 section. The influence on lateral displacements in inducing different mechanisms will be discussed later in Section 4.2.

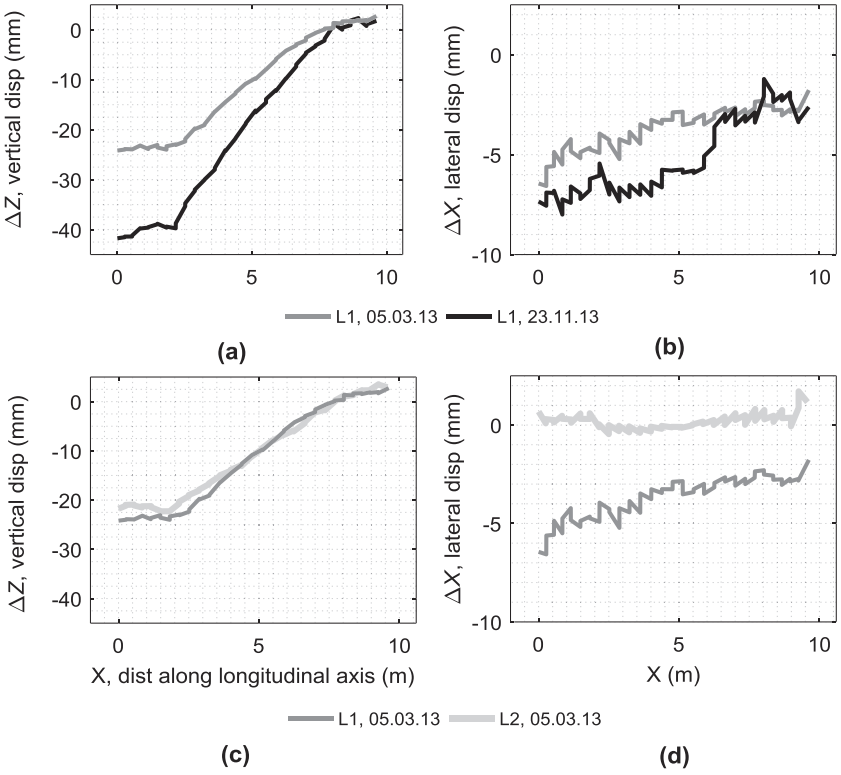

Fig. 13. Vertical and horizontal displacements obtained by applying the proposed IPAM method to different point cloud slices from different dates. (a)-(b) Displacement response 'during' and 'after' piling for slice L1 is shown alongside (c)-(d) a comparison of displacement response 'during' piling for slices L1 and L2.

The continuous deformation profiles provided by the proposed IPAM method are useful for evaluating the serviceability criteria, which concern changes in vertical track alignment induced as a result of support movements. The most significant differential vertical movements are observed in the after piling stage for L1. Here, a differential settlement of 40 mm is observed between the hinge locations at $X = 2.15$ and $X = 8$ m. This corresponds to a change in gradient of approximately 0.45 degrees. This is a conservative estimate of track vertical alignment change, the presence of fill and ballast above the vault would result in smaller values. This change is not considered critical for the operation of trains.

Track cant describes the elevation difference between the two rails on a track and twist describes the change of cant along the track. Due to the two-dimensional response, it is expected that changes in track cant and twist will be minimal. In particular, for assessing the changes in cant, the vertical displacements at crown can be explored. There is significantly less fill over the crown (as opposed to the springings), therefore the crown vertical displacements would more closely reflect vertical displacements at the track level. By investigating the crown response along the transverse length of the arch in Fig. 14, it can be observed that the displacements are fairly uniform. Along the arch, the largest differential settlements over a 1.4 m gauge would be approximately 3 mm (between the coordinates $Y = 10.7 - 12.1$ m) which would correspond to a cant change of 0.1 degrees. This change would not be considered significant in terms of serviceability, and no remedial work would be necessary.

4.2. Simple modelling of structural response

The support movements of Arch E57 did not affect the serviceability of the track. Therefore, reliably assessing the structural damage of the vault remains the main concern. In this section, the arch response to settlements is described with simple mechanical models.

The deformation profiles presented in Section 4.1 demonstrated that the arch was responding as a 2D mechanism in its longitudinal direction, therefore the damage is expected to concentrate in this direction. To model this behaviour, classical limit analysis assumptions may be utilised [33]. These assumptions are (i) masonry does not exhibit sliding and (ii) it has infinite compressive strength and (iii) zero tensile strength. As a result, the loads are transferred through the structure via a thrust line. To sustain support movements, thrust line migrates to the intrados and extrados of the arch, forming hinges. These hinges provide rotational releases, leading to a kinematic mechanism, where assemblies of rigid bodies rotate with respect to one another.

To identify the kinematic mechanism of the arch, the commercial software RING by Limit State is utilised. In this software, force equilibrium of the settling arch is formulated at each contact. This equilibrium is subject to a number of constraints, which relate to the limit analysis assumptions. There exists an infinite number of equilibrium states, which can satisfy these constraints. However, when an additional constraint which minimises the work done by support forces for a virtual support displacement is specified, a unique equilibrium state can be determined. For further details concerning the mathematical formulation used in identifying this mechanism, refer to [34].

The unique state which describes the equilibrium response of the settling arch corresponds to a kinematic mechanism which features support movements. It is not possible to predict the small displacements prior to this point [35], however, the following displacements can be estimated with kinematic analyses [5,6,36]. In these analyses, macro blocks which are located between these hinges are assumed rotate. To find the unknown rotation of these blocks, small displacement theory is used. According to this theory, the known horizontal and vertical differential support movements Δp_h and Δp_v (from the experienced or predicted displacements) may be described as a function of the original hinge coordinates (for hinge *i*, these coordinates are X_i and Y_i) and the unknown absolute rotations (for macro block *j*, this rotation is denoted by θ_j). This typically results in a system of one or two equations with one or two unknowns, which has a unique solution. This system can be expressed in matrix notation as follows:

$$\mathbf{p} = \begin{bmatrix} \Delta\mathbf{Y} \\ -\Delta\mathbf{X} \end{bmatrix} \theta \tag{2}$$

where the differential support settlement matrix is defined as $\mathbf{p} = [\Delta p_h, \Delta p_v]^T$. The other matrices in Eq. (2) are expressed differently for different cases. When there are two hinges, there is only a single macro block rotating and $\theta = [\theta_1]$, $\Delta\mathbf{X} = [X_2 - X_1]$ and $\Delta\mathbf{Y} = [Y_2 - Y_1]$. For the case where three hinges are identified and two macro-blocks rotate, the parameters are expressed as $\theta = [\theta_1, \theta_2]^T$, $\Delta\mathbf{X} = [X_2 - X_1, X_3 - X_2]$ and $\Delta\mathbf{Y} = [Y_2 - Y_1, Y_3 - Y_2]$. Finally, a five hinge mechanism indicates the rotation of four macro blocks. However, these rotations cannot be uniquely solved with the information provided. In this case, it is assumed that the 1st and 5th hinges do not rotate, and the rotation at the other hinges is identified using Eq. (2). Therefore, the parameters can be given as follows: $\theta = [\theta_2, \theta_3]^T, \Delta\mathbf{X} = [X_3 - X_2, X_4 - X_3]$ and $\Delta\mathbf{Y} = [Y_3 - Y_2, Y_4 - Y_3]$.

The kinematic analysis of arch displacements in response to support movements is conducted using the geometry of Arch E57, which was presented earlier in Fig. 2. Analyses were conducted for two specific cases. In the first case, the response of L1 after piling is modelled. In the second case, the response of L2 during piling is modelled. The support movements which were used

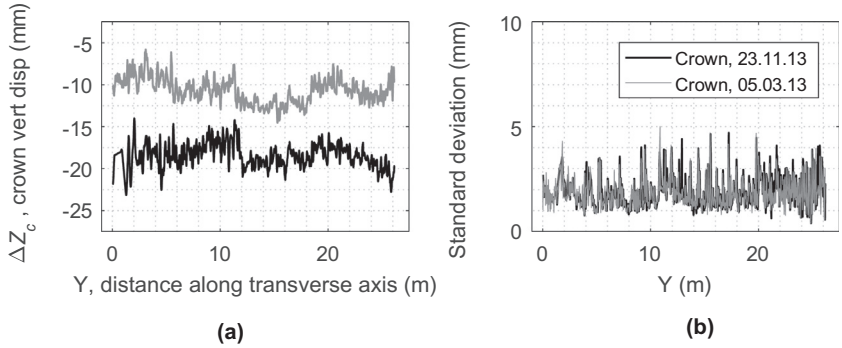

Fig. 14. (a) Vertical displacements estimated for the crown during piling on 05.03.13 and after piling on 23.11.13 using the M3C2 method (data is filtered) and (b) standard deviation of points used in M3C2 analyses.

for the analyses were determined from the total station data. The vertical and horizontal displacement profiles of the intrados of the arch obtained from these analyses are compared with proposed IPAM results in Fig. 15.

The model results and the IPAM data in Fig. 15 demonstrate a good agreement. In particular, all vertical displacement traces feature three straight lines with different slopes. It is noteworthy that all of the analyses and the IPAM results indicate the formation of an extrados hinge at $X = 2.15$ m. Fig. 2 indicates that this hinge is located at the upper end of the backing above the piers. In addition, the analyses indicate another hinge formation on the eastern side of the arch. In Fig. 15a, this intrados hinge is observed at $X = 7.2$ m, and in Fig. 15c, it is observed at $X = 8.2$ m. A qualitatively similar phenomenon is observed in the IPAM data, although the indicated hinge locations are closer to the eastern springing point.

The lateral displacement traces predicted by analyses and estimated by IPAM are also presented in Fig. 15. The results are similar, and the analyses predict the observed displacements with millimetric accuracy. In particular, the sudden jump in the lateral displacement trace at the coordinate $X = 2.15$ m refers to crack opening in the extrados hinge. In Fig. 15b and 15d, respective jumps of 5 mm and 2.5 mm are recorded. A smaller jump in the traces is observed for the IPAM data around the same location. A potential reason for this disagreement may be due to the diffuse hinging in the arch, or the displacement continuity that is enforced in the IPAM method (see Section 3.2).

4.3. Assessment of settlement-induced damage

For planning ground works (e.g. open excavation, tunnelling) near vaulted masonry structures, an assessment of settlement-induced structural damage is often necessary. As discussed earlier in Section 1, it is desirable to propose simple models, which can provide a preliminary but relevant indication of this damage. Section 4.2 proposed the use of simple limit analyses of masonry arches to estimate the longitudinal response of a settling masonry arch in lieu of elastic deep beam models. The improved agreement between the field displacement data and the analyses validated the ability of limit analyses to capture structural response to settlements. In this section, the limit analysis modelling technique is used to quantify damage in a masonry vault for a range of support movement scenarios.

For preliminary analyses, settlement-induced damage can be quantified by evaluating how easy it is to repair the observed damage. In his seminal work, Burland [1] correlated this notion of 'ease of repair', with the size and extent of cracking that is observed in a structure. According to this approach, in the case of very slight damage, fine cracks, smaller than 1 mm in width, are observed. These cracks can be easily treated. However, in the case of moderate damage, up to 15 mm cracking may be observed, which might affect weathertightness and will require repointing. This standard and preliminary definition of damage for buildings is also utilised herein for masonry arch bridges. While a dedicated consideration of ease of repair would be useful for masonry arch bridges, using Burland's damage assessment tables is sufficient for a preliminary damage classification. This is particularly true for negligible to moderate levels of damage where the cracking is small and repairs are related to local fixes to cracks and drainage systems.

Using the limit analyses, it is possible to determine the crack opening in a simple manner. Crack opening can be defined as the relative rotation in a joint (rotation between bricks or stone voussoirs in a hinge) multiplied by the total depth of the arch. For instance, for the slice L1 which was examined earlier in Fig. 15, the maximum relative rotation between segments is determined as 0.45° after piling. This corresponds to a crack opening of approximately 6 mm at the extrados hinge, which can be classified as moderate damage.

For the investigated Arch E57, a number of hypothetical cases can be explored to determine the influence of different support movements on the arch response mechanisms. This is explored in Fig. 16. The investigated cases include the arch span closing and opening (Cases 1 & 6), arch settling vertically (Case 2) and a combination of these support movements (Cases 3–5). In this fig-

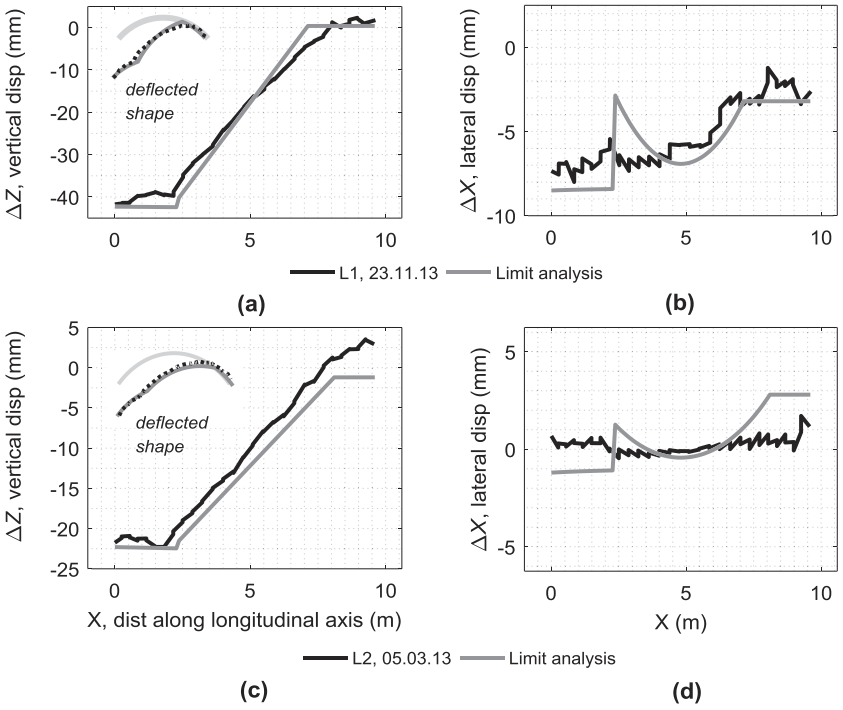

Fig. 15. Vertical and horizontal displacements obtained by applying the proposed IPAM method to the 'point cloud slices and by kinematic mechanism analyses. (a)-(b) Displacement response 'during' and 'after' piling for slice L1 is shown alongside (c)-(d) a comparison of response 'during' piling for slices L1 and L2.

ure, the vertical and horizontal differential support movements are denoted by Δp_h and Δp_v (in mm), while the maximum magnitude of the relative rotation at any hinge (rotation between separating brick or voussoirs) is given by $\max(|\Delta\theta_{rel}|)$ (in °). The identified mechanism is independent of the magnitude of displacements Δp_h and Δp_v (see Section 3 for a description of how the mechanism is determined in the RING software), however, their ratio is critical. Therefore, specifying a vertical differential displacement of 1 mm or 5 mm vertical displacement yields the same mechanism, but with different relative rotation and crack opening. In Fig. 16, a total relative support displacement of 1 mm was applied for each case and this was partitioned between horizontal and vertical support movements. Within this context, a value of $\Delta p_h = -1$ for Case 1 shows −1 mm of arch span closing due to horizontal movements, with no relative vertical support movement. In the deflected shape representations, the dots show the hinge locations and the line inside the arch shows the calculated thrust line.

Fig. 16 covers support movement scenarios which were investigated earlier in the paper for sections L1 and L2. These are similar to Cases 3 and 4, where the arch is primarily settling, but the arch span is opening (e.g. piers are spreading) at the same time. Upon inspection, it can be observed that hinge locations vary significantly to allow for different support movements, and this causes changes in the expected crack opening. Two other cases, Cases 5 and 6, discuss the arch span opening response. Case 5 is interesting as it demonstrates that the support movements may be accommodated with only two hinges. Case 6 shows the well-known three hinge span opening mechanism where intrados hinges are located at springing points and the extrados hinge is located at the crown. This mechanism engages the whole arch and causes maximum relative rotations of 0.02 degrees at the extrados hinge for 1 mm span opening.

In contrast, Cases 1 and 2 of Fig. 16, where the span closing is dominant, demonstrate a five hinge mechanism instead of the well-known 3 hinge closing mechanism [33]. This difference may be due to a modelling assumption. In the Limit State Ring software, an extrados hinge will not form at levels where the arch is supported by backing. As a result of this, the hinge migrates to the top of the backing level. Therefore, large rotations need to be activated to accommodate support movements and the indicated hinge rotations for Cases 1 and 2 are an order of magnitude higher than the other cases. This finding indicates that span closing is potentially the most damaging support movement for the masonry arch. However, further field data is required to validate these models. Alternative response mechanisms which involve the rigid body rotation of the stiff pier top and which are not considered by limit analysis software, may be activated during support movements [37].

Fig. 16 demonstrated that it is possible to conservatively quantify the damage in Arch E57 for a range of support movements. This is achieved with a new damage map in Fig. 17. Here, the damage is assumed to be correlated with the maximum crack opening. An upper bound of 1, 5, 15 and 25 mm crack opening is specified for very slight, slight, moderate and severe damage states according to Burland's damage assessment method [1]. Then, the support movements which cause these damage states are identified using the limit analyses for different combinations of support movements. These include the cases examined in Fig. 16, which are highlighted with magenta data points in Fig. 17. More specifically, these points show the horizontal strain and deflection ratios required to cause severe damage for the generic combination of support movements indicated in Fig. 16. It is useful to note that the non-dimensional deflection ratio and horizontal strain

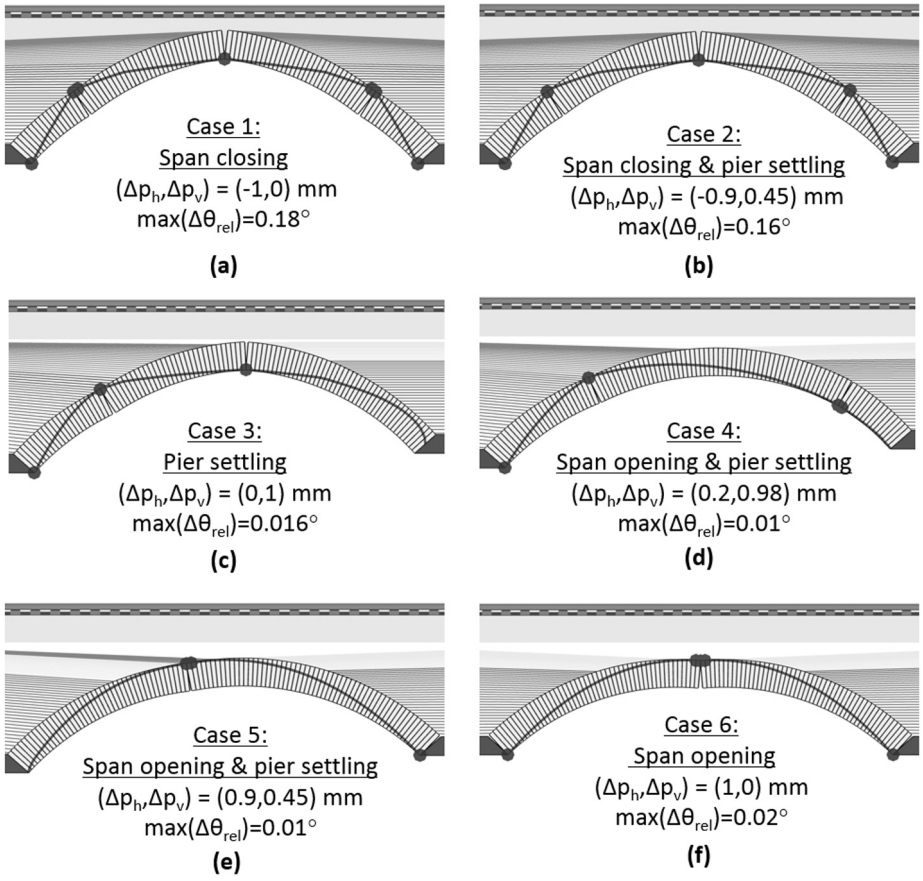

Fig. 16. Schematic representation of the mechanism analysis of Arch E57 for different scenarios of support movements.

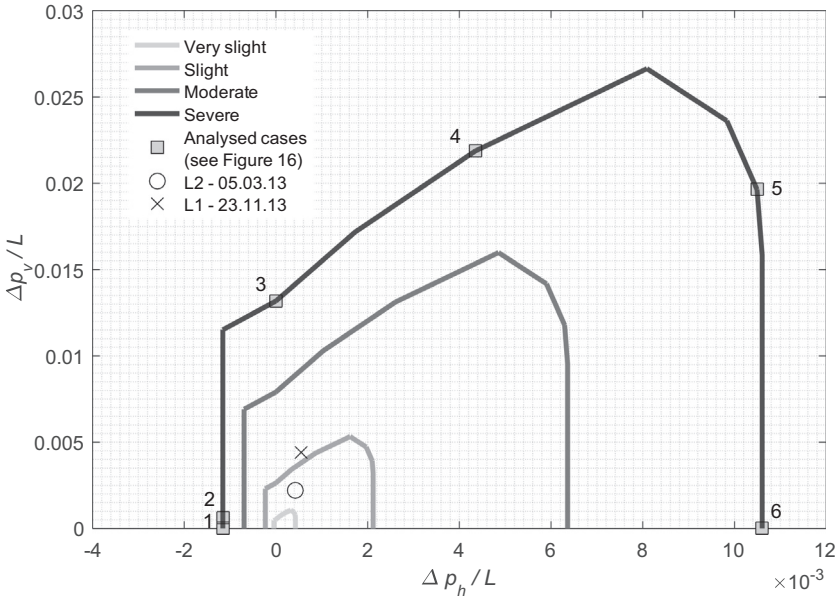

Fig. 17. Damage prediction maps produced using limit analyses which correlate damage states to different scenarios of support movements, described by deflection ratio and horizontal strain parameters.

parameters were defined earlier in Section 2. Deflection ratio is defined as relative vertical support displacement normalised by span, $\frac{\Delta p_v}{L}$ while, the horizontal strain is defined as relative horizontal support movement normalised by span $\frac{\Delta p_h}{L}$.

The damage map quantifies the dominating influence of horizontal support movements in dictating the response mechanisms. This is particularly true for negative horizontal strains (arch span closing). Cases 1 and 2 in Fig. 16 experienced similar mechanisms, despite the significant vertical movements in Case 2. In addition, many different response mechanisms are identified for the combination of span opening and vertical settlement cases. In addition, Fig. 17 demonstrates that the arch can accommodate larger support movements for particular combinations of horizontal and vertical displacements than for purely vertical displacements. Finally, two data points on Fig. 17 describe the damage predictions for Arch E57. These indicate that the damage progresses from slight to moderate with the progression of piling works. If these predicted damage states are contrasted with the 'very slight' damage state obtained using the existing assessment techniques (see Section 2), the improved accuracy of the proposed assessment technique can be noted.

5. Conclusions

This paper developed new monitoring and assessment techniques to describe the influence of support movements on the structural response of masonry vaults. First, point cloud monitoring techniques were explored. The main advantage of these methods over existing monitoring techniques is their ability to provide continuous deformation profiles. It was determined that the M3C2 method, which calculates the distance between point clouds, was reliable when calculating the surface normal movements of flat objects. Therefore the M3C2 method was used to calculate the lateral movement of piers in the longitudinal plane and vertical movement profiles at the crown in the transverse plane. In addition, a new method called the IPAM method was developed for determining the three dimensional displacement fields to describe the longitudinal response of the vault. New information concerning track deformations and vault kinematic mechanisms could be gathered using this new method, enabling the reliable estimation of serviceability and damage states on the basis of monitoring data.

Simple limit analysis models were used to simulate the critical longitudinal settlement response of vaults. The comparisons between the model results and the IPAM derived movement data suggested a good agreement. The analysis results were then generalised by modelling a range of support movement scenarios, and plotting them in assessment maps which quantify damage for any given support movement. The ability of these maps to reliably estimate the emerging crack magnitudes for the investigated cases represented a marked improvement on the existing preliminary assessment techniques.

While the current paper proposes a new method to observe displacements of the vault using multiple point clouds gathered during the settlements, sometimes this data is not available. In particular, when assessing masonry bridges, engineers often have to understand the influence of past settlements on the load carrying capacity of a masonry arch. For this purpose, the authors' ongoing work investigates inferring past support displacements from the distorted arch geometry obtained from a single point cloud of the structure.

Acknowledgements

The work carried out was funded by EPSRC and Innovate UK, through the Cambridge Centre for Smart Infrastructure and Construction (Grant Reference Number EP/L010917/1). The research materials supporting this publication can be accessed at https://doi.org/10.17863/CAM.10421. The authors would like to thank Vincent Auzel of Soldata and Dean Bain and Tim Delbaere of Costain who provided the raw monitoring data that was used in this study.

References

[1] J.B. Burland, C.P. Wroth, Settlement of buildings and associated damage, Settl. Struct. Proc. Conf. Br. Geotech. Soc., Pentech Press, London, 1974, pp. 611–764.
[2] M.D. Boscardin, E.J. Cording, Building response to excavation induced settlement, J. Geotech. Eng. 115 (1989) 1–21.
[3] Z. Orban, Assessment, Reliability and Maintenance of Masonry, in: P. Roca, C. Molins (Eds.), Arch Bridge. IV-Advances Assessment, Struct. Des. Constr., Barcelona, 2004, pp. 152–161.

[4] J. Ochsendorf, Collapse of Masonry Structures, University of Cambridge, 2002.
[5] J. Zessin, W.W. Lau, J.A. Ochsendorf, Equilibrium of cracked masonry domes, Eng. Comput. Mech. 163 (2010) 135–145.
[6] J. McInerney, M. DeJong, Discrete element modeling of groin vault displacement capacity, Int. J. Archit. Herit. 9 (2015) 1037–1049.
[7] H. Mohamad, P.J. Bennett, K. Soga, R.J. Mair, K. Bowers, Behaviour of an old masonry tunnel due to tunnelling-induced ground settlement, Géotechnique 60 (2010) 927–938.
[8] S. Atamturktur, L. Bornn, F. Hemez, Vibration characteristics of vaulted masonry monuments undergoing differential support settlement, Eng. Struct. 33 (2011) 2472–2484.
[9] S. Prabhu, S. Atamturktur, D. Brosnan, P. Messier, R. Dorrance, Foundation settlement analysis of fort sumter national monument: model development and predictive assessment, Eng. Struct. 65 (2014) 1–12.
[10] D. Watt, B. Colston, Investigating the effects of humidity and salt crystallisation on medieval masonry, Build. Environ. 35 (2000) 737–749.
[11] A. Tomor, E. Verstrynge, A joint fatigue-creep deterioration model for masonry with acoustic emission based damage assessment, Constr. Build. Mater. 43 (2013) 575–588.
[12] J. Richmond, J. Parker, M. Sharratt, The Shard, London, UK: response of arches to ground movements, Proc. ICE-Bridge Eng. 165 (2012) 185–194.
[13] M.S. Acikgoz, L. Pelecanos, G. Giardina, J. Aitken, K. Soga, Distributed sensing of a masonry vault during nearby piling, Struct. Control Heal. Monit. 24 (2017) e1872.
[14] C. Camos, O. Spackova, D. Straub, C. Molins, Probabilistic approach to assessing and monitoring settlements caused by tunneling, Tunn. Undergr. Sp. Technol. 51 (2016) 313–325.
[15] A. Pesci, G. Casula, E. Boschi, Laser scanning the Garisenda and Asinelli towers in Bologna (Italy): detailed deformation patterns of two ancient leaning buildings, J. Cult. Herit. 12 (2011) 117–127.
[16] D. Lague, N. Brodu, J. Leroux, Accurate 3D comparison of complex topography with terrestrial laser scanner: application to the Rangitikei canyon (N-Z), ISPRS J. Photogramm. Remote Sens. 82 (2013) 10–26.
[17] G. Teza, A. Galgaro, N. Zaltron, R. Genevois, Terrestrial laser scanner to detect landslide displacement fields: a new approach, Int. J. Remote Sens. 28 (2007) 3425–3446.
[18] Alan Baxter Associates, London Bridge Station Structural Investigation: Interpretative Report, N231–32112-ALB-REP-ST-000027. London, 2011.
[19] Hyder-WSP, London Bridge Station Development train shed demolition Network Rail emergency preparedness plan, N420-COT-ERP-CS_000004. London, 2012.
[20] M.J. Westoby, J. Brasington, N.F. Glasser, M.J. Hambrey, J.M. Reynolds, "Structure-from-motion" photogrammetry: a low-cost, effective tool for geoscience applications, Geomorphology 179 (2012) 300–314.
[21] S. AlKkheder, Y. Al-Shawabkeh, N. Haala, Developing a documentation system for desert palaces in Jordan using 3D laser scanning and digital photogrammetry, J. Archaeol. Sci. 36 (2009) 537–546.
[22] N. Hallermann, G. Morgenthal, V. Rodehorst, Vision-based monitoring of heritage monuments: Unmanned Aerial Systems (UAS) for detailed inspection and high-accuracy survey of structures, WIT T. Built Environ. 153 (2015) 621–632.
[23] B. Riveiro, P.B. Lourenço, D.V. Oliveira, H. González-Jorge, P. Arias, Automatic Morphologic Analysis of Quasi-Periodic Masonry Walls from LiDAR, Comput. Civ. Infrastruct. Eng. 31 (2016) 305–319.
[24] B. Riveiro, M.J. DeJong, B. Conde, Automated processing of large point clouds for structural health monitoring of masonry arch bridges, Autom. Constr. (2016).
[25] L. Schueremans, B. Van Genechten, The use of 3D-laser scanning in assessing the safety of masonry vaults-A case study on the church of Saint-Jacobs, Opt. Lasers Eng. 47 (2009) 329–335.
[26] J. Armesto-González, B. Riveiro-Rodríguez, D. González-Aguilera, M.T. Rivas-Brea, Terrestrial laser scanning intensity data applied to damage detection for historical buildings, J. Archaeol. Sci. 37 (2010) 3037–3047.
[27] G. Teza, A. Pesci, Geometric characterization of a cylinder-shaped structure from laser scanner data: development of an analysis tool and its use on a leaning bell tower, J. Cult. Herit. 14 (2013) 411–423.
[28] B. Van Genechten, T. Demeyere, S. Herinckx, J. Goos, L. Schueremans, D. Roose, et al., Terrestrial Laser Scanning in Architectural Heritage – Deformation Analysis and the Automatic Generation of 2D Cross- Sections, in: Proc. CIPA XXII Int. Symp. Digit. Doc. Interpret. Present. Cult. Herit., Kyoto, 2009.
[29] A. Soni, S. Robson, B. Gleeson, Structural monitoring for the rail industry using conventional survey, laser scanning and photogrammetry, Appl. Geomatics 7 (2015) 123–138.
[30] P.J. Besl, Neil D. McKay, Method for registration of 3-D shapes, in: Proc. SPIE 1611, Sensor Fusion IV: Control Paradigms and Data Structures, vol. 586, 1992, pp. 127–134.
[31] H.M. Kjer, J. Wilm, Evaluation of Surface Registration Algorithms for PET Motion Correction, Technical University of Denmark, 2010.
[32] S. Rusinkiewicz, M. Levoy, Efficient variants of the ICP algorithm, in: Proceedings Third International Conference on 3-D Digital Imaging and Modeling, Quebec City, Que., 2001, pp. 145–152.
[33] J. Heyman, The stone skeleton, Int. J. Solids Struct. 2 (1966) 249–279.
[34] LimitState Ltd, LimitState: RING Manual Version 3.1b, 2014.
[35] F. Portioli, L. Cascini, Assessment of masonry structures subjected to foundation settlements using rigid block limit analysis, Eng. Struct. 113 (2016) 347–361.
[36] S. Coccia, F. Di Carlo, Z. Rinaldi, Collapse displacements for a mechanism of spreading-induced supports in a masonry arch, Int. J. Adv. Struct. Eng. 7 (2015) 307–320.
[37] B. Harvey, Stiffness and damage in masonry bridges, Proc. ICE-Bridge Eng. 165 (2012) 127–134.